

Facile, One-Pot Synthesis of Pd@Pt Octahedra with Enhanced Activity and Durability toward Oxygen Reduction

Ming Zhou, Helan Wang, Ahmed O. Elnabawy, Zachary D. Hood, Miaofang Chi, Peng Xiao, Yunhuai Zhang, Manos Mavrikakis, and Younan Xia

Chem. Mater., Just Accepted Manuscript • DOI: 10.1021/acs.chemmater.8b04756 • Publication Date (Web): 18 Jan 2019

Downloaded from <http://pubs.acs.org> on January 19, 2019

Just Accepted

“Just Accepted” manuscripts have been peer-reviewed and accepted for publication. They are posted online prior to technical editing, formatting for publication and author proofing. The American Chemical Society provides “Just Accepted” as a service to the research community to expedite the dissemination of scientific material as soon as possible after acceptance. “Just Accepted” manuscripts appear in full in PDF format accompanied by an HTML abstract. “Just Accepted” manuscripts have been fully peer reviewed, but should not be considered the official version of record. They are citable by the Digital Object Identifier (DOI®). “Just Accepted” is an optional service offered to authors. Therefore, the “Just Accepted” Web site may not include all articles that will be published in the journal. After a manuscript is technically edited and formatted, it will be removed from the “Just Accepted” Web site and published as an ASAP article. Note that technical editing may introduce minor changes to the manuscript text and/or graphics which could affect content, and all legal disclaimers and ethical guidelines that apply to the journal pertain. ACS cannot be held responsible for errors or consequences arising from the use of information contained in these “Just Accepted” manuscripts.



ACS Publications

is published by the American Chemical Society, 1155 Sixteenth Street N.W., Washington, DC 20036

Published by American Chemical Society. Copyright © American Chemical Society. However, no copyright claim is made to original U.S. Government works, or works produced by employees of any Commonwealth realm Crown government in the course of their duties.

Facile, One-Pot Synthesis of Pd@Pt_{1L} Octahedra with Enhanced Activity and Durability toward Oxygen Reduction

Ming Zhou,^{†,‡,§} Helan Wang,^{†,+,§} Ahmed O. Elnabawy,^{||,§} Zachary D. Hood,^{¶,‡} Miaofang Chi,[‡] Peng Xiao,[‡] Yunhuai Zhang,[‡] Manos Mavrikakis,^{||,*} and Younan Xia^{†,¶,*}

[†]The Wallace H. Coulter Department of Biomedical Engineering, Georgia Institute of Technology and Emory University, Atlanta, Georgia 30332, United States

^{||}Department of Chemical and Biological Engineering, University of Wisconsin–Madison, Madison, Wisconsin 53706, United States

[‡]College of Chemistry and Chemical Engineering, Chongqing University, Chongqing 400044, China

[¶]School of Chemistry and Biochemistry, School of Chemical and Biomolecular Engineering, Georgia Institute of Technology, Atlanta, Georgia 30332, United States

^{*}College of Chemistry, Chemical Engineering and Biotechnology, Donghua University, Shanghai 201620, China

^{||}Center for Nanophase Materials Sciences, Oak Ridge National Laboratory, Oak Ridge, Tennessee 37831, United States

[§]These authors contributed equally to this work.

^{*}Corresponding authors: manos@engr.wisc.edu (for computation) and younan.xia@bme.gatech.edu (for synthesis and electrochemical characterization)

1
2
3
4
5
6
ABSTRACT

7
8
9
10
11
12
13
14
15
16
17
18
19
20
21
22
23
24
25
26
27
28
29
30
31
32
33
34
35
36
37
38
39
40
41
42
43
44
45
46
47
48
49
50
51
52
53
54
55
56
57
58
59
60
A successful strategy for reducing the content of Pt without compromising the activity of a Pt-based catalyst is to deposit Pt as an ultrathin overlayer on the surface of another metal. Here we report a facile, one-pot synthesis of $\text{Pd}@\text{Pt}_{1\text{L}}$ (1L: one atomic layer) core-shell octahedra using a solution-phase method. The success of this method relies on the use of metal precursors with markedly different reduction kinetics. In a typical synthesis, the ratio between the initial reduction rates of the $\text{Pd}(\text{II})$ and $\text{Pt}(\text{II})$ precursors differed by almost 100 times, favoring the formation of Pd-Pt bimetallic octahedra with a core-shell structure. The reduction of the $\text{Pt}(\text{II})$ precursor at a very slow rate and the use of a high temperature allowed the deposited Pt atoms to spread and cover the entire surface of Pd octahedral seeds formed in the initial stage. More importantly, we were able to scale up this synthesis using continuous-flow reactors without compromising product quality. Compared to a commercial Pt/C catalyst, the $\text{Pd}@\text{Pt}_{1\text{L}}$ core-shell octahedra showed major augmentation in terms of catalytic activity and durability for the oxygen reduction reaction (ORR). After 10,000 cycles of accelerated durability test, the core-shell octahedra still exhibited a mass activity of $0.45 \text{ A mg}^{-1}\text{Pt}$. We could rationalize the experimental results using density functional theory (DFT) calculations, including the mechanism of synthesis, ORR activities, and possible Pd-Pt atom swapping to enrich the outermost layer with Pd. Specifically, the as-synthesized $\text{Pd}@\text{Pt}_{1\text{L}}$ octahedra tended to take a slightly mixed surface composition because the deposited Pt atoms were able to substitute into Pd upon deposition on the edges; ORR energetics were more favorable on pure Pt shells as compared to significantly mixed Pd-Pt shells; and the activation energy barriers calculated for the Pd-Pt atom swapping were too prohibitive to significantly alter the surface composition of the as-synthesized $\text{Pd}@\text{Pt}_{1\text{L}}$ octahedra, helping sustain their activity for prolonged operation.

INTRODUCTION

One of the major concerns faced by the proton exchange membrane fuel cells (PEMFCs) is the need to load a large amount of the Pt-based catalyst on the cathode to speed up the sluggish kinetics associated with the oxygen reduction reaction (ORR).¹⁻³ Given the low abundance, ever increasing cost, and sustainability issues associated with a precious metal such as Pt, it is not difficult to understand why it has been a challenging task to market the PEMFC technology on an industrial scale.⁴⁻⁶ A viable strategy for mitigating this issue is to increase the utilization efficiency of Pt by engineering the surface structure through a facet-controlled synthesis, and thereby reduce the Pt content.⁷⁻⁹ To this end, various methods have been explored to improve the specific and mass activities of Pt-based catalysts.¹⁰⁻¹³ One of the promising strategies is to deposit Pt atoms as an one-atom-thick shell on nanoparticles made of a more abundant and/or less expensive metal.¹⁴⁻²¹ In particular, it has been demonstrated that monolayers or sub-monolayers of Pt could be deposited on nanoparticles made of Pd or other metals (as well as their alloys with Pt) *via* a galvanic replacement process that involves the under-potential deposition (UPD) of Cu shell.^{15,16} Catalysts prepared using this approach showed greatly enhanced mass activity toward ORR. In addition, ultrathin skins of Pt were formed on the surfaces of nanoparticles made of Pt₃Ni, Pt₃Co, PtCu, or WC through annealing, dealloying, or high-temperature self-assembly to obtain catalysts with enhanced activities.¹⁷⁻²⁰ Most recently, our groups synthesized Pd@Pt core-shell nanocrystals featuring different surface structure through chemical deposition of Pt shells on Pd nanocrystal seeds with cubic, octahedral, and icosahedral shapes, respectively.^{10,14,21} The thickness of the Pt shells could be increased from a few to six atomic layers, and catalysts based on the resultant core-shell nanocrystals showed significantly enhanced activity and durability when benchmarked against a state-of-the-art Pt/C catalyst. In general, it has been a challenging task to scale up the production of nanocrystal-based catalysts without compromising the quality control although these prior studies have clearly validated the feasibility to generate advanced electrocatalysts by coating ultrathin Pt shells on nanocrystals made of another metal.

One-pot synthesis can potentially alleviate some of the issues associated with the quantity, time, and cost of a catalytic system. Owing to its promise for scale-up production, one-pot route has received considerable interest.²²⁻²⁴ In a recent demonstration, we established that Pt could be coated as conformal and uniform shells on Pd octahedral nanocrystals in a one-pot synthesis by quantitatively manipulating the ratio between the initial reduction rates of two precursors based

upon PdCl_4^{2-} and PtCl_4^{2-} .²⁵ When a relatively high reaction temperature of 160 °C was used, the deposited Pt atoms were able to diffuse across the entire surface of a Pd nanocrystal, generating a Pt shell through a layer-by-layer growth pathway. However, because the initial reduction rates of the two metal precursors only differed by about 10 times, it was difficult to obtain $\text{Pd}@\text{Pt}$ core-shell nanocrystals with a monolayer or sub-monolayer coverage for the Pt shells. In separate studies, it was established that $\text{Pt}(\text{acac})_2$ could be reduced at a much slower rate relative to that of PtCl_4^{2-} owing to a relatively strong complexation of the acac ligand to Pt^{2+} .^{26,27} As such, it is interesting to examine if one can generate Pt monolayer coating by replacing PtCl_4^{2-} with $\text{Pt}(\text{acac})_2$. In addition, it is more attractive to use $\text{Pt}(\text{acac})_2$ rather than PtCl_4^{2-} as the Cl^- ions contained in the later complex can facilitate oxidative etching, leading to a detrimental inter-diffusion process between Pd and Pt atoms, and thus the formation of alloys.²⁸ Taken together, it should be advantageous to extend the one-pot protocol by switching the precursor from PtCl_4^{2-} to $\text{Pt}(\text{acac})_2$ for the facile synthesis of $\text{Pd}@\text{Pt}_{\text{IL}}$ core-shell nanocrystals.

Herein, we demonstrate a one-pot method by judiciously choosing the right precursors for Pd and Pt to temporally separate their reduction into two steps, even though both of the precursors are presented in the same reaction solution. The success of our synthesis relies on the choice of two precursors with markedly different reduction rates. As such, by precisely manipulating the amount of the Pt precursor added, we are able to deterministically generate $\text{Pd}@\text{Pt}_{\text{IL}}$ core-shell nanocrystals with an octahedral shape for the development of ORR catalysts with substantially enhanced activities. More significantly, we have quantitatively analyzed the kinetics responsible for the formation of $\text{Pd}@\text{Pt}_{\text{IL}}$ core-shell nanocrystals. We are also able to scale up the synthesis using continuous flow reactors without compromising the product quality. We augmented this with a DFT study of the diffusion mechanism of the deposited Pt atoms on the edges of Pd octahedra, as well as Pt-Pd swapping at the interface between the Pt_{IL} shell and the Pd core. Our calculations explained the reliable experimentally-observed stability of the $\text{Pd}@\text{Pt}_{\text{IL}}$ core-shell octahedra.

EXPERIMENTAL SECTION

Chemicals and Materials. While ethylene glycol (EG, lot no. L05B13) was ordered from J. T. Baker, all other chemicals, including sodium tetrachloropalladate(II) (Na_2PdCl_4 , 99.998%), platinum(II) acetylacetone ($\text{Pt}(\text{acac})_2$, 98%), L-ascorbic acid (AA), poly (vinyl pyrrolidone) (PVP, MW≈55000), acetic acid (99.7%), hydrochloric acid (HCl, 37%), perchloric acid (HClO_4 ,

70%, PPT grade, Veritas), and ethanol (Pharmco Products, 200 proof), were purchased from Sigma-Aldrich. The chemicals were used as received. We used deionized (DI) water with a resistivity of 18.2 MΩ cm at room temperature to prepare all the aqueous solutions.

Synthesis of Pd@Pt_{1L} Core-Shell Octahedra. The Pd@Pt_{1L} octahedra were synthesized by adding a solution of Na₂PdCl₄ and Pt(acac)₂ in EG into another solution of PVP and AA in EG through the use of a pipet. In the standard protocol, 50 mg of AA and 50 mg of PVP were mixed in 7 mL of EG held in a vial at room temperature. The mixture was magnetically stirred for 10 min to ensure complete dissolution. Afterwards, 3 mL of another solution (in EG) containing 38.2 mg of Na₂PdCl₄ and 15 mg of Pt(acac)₂ was injected with a pipet and the final mixture was kept under magnetic stirring for another 10 min under ambient conditions. The mixture was then subjected to heating in an oil bath held at 160 °C. After 3 h, the vial was taken out and naturally cooled down to room temperature. Typically, we collected the product through centrifugation at 55000 rpm, followed by washing with acetone once and with DI water twice. The final solid was re-dispersed in 10 mL of DI water.

Synthesis of Pd@Pt_{1L} Core-Shell Octahedra in Continuous Flow Reactors. In a typical process, 38.2 mg of Na₂PdCl₄, 15 mg of Pt(acac)₂, 50 mg of AA, and 50 mg of PVP were mixed in 10 mL of EG hosted in a vial under ambient conditions with the assistance of magnetic stirring. The mixture was then heated to 80 °C for 10 min to ensure the dissolution of all the solids. Afterward, the solution was cooled down to room temperature prior to its introduction into a fluidic device that was assembled from a PTFE tube with an inner diameter of 1.58 mm (typically used at a length of 7.5 m), a syringe, and a syringe pump, as illustrated in Figure S1. In a standard protocol, the PTFE tube was immersed in an oil bath held at 160 °C and the fluidic system was operated at a flow rate of 0.3 mL min⁻¹. The residence time, defined by the length of the PTFE tube and the flow rate, was typically set to 30 min. The solution containing the solid products was collected in a centrifuge tube. After cooling down to room temperature, the solid products were precipitated out by adding 30 mL of acetone into the 10 mL of as-obtained solution. After centrifugation at 12000 rpm for 10 min, the supernatant was discarded and the solid products were washed twice with water. The resulting Pd@Pt_{1L} core-shell octahedra could be easily re-dispersed in 10 mL of water. Figure S2 shows a typical TEM image of the solid products. The Pd/Pt molar ratio for the Pd@Pt_{1L} core-shell octahedra was 3.51, as indicated by ICP-MS analysis. All samples of Pd@Pt_{1L}

1
2
3 core-shell octahedra used for the electrochemical characterizations were produced using the fluidic
4 system, unless otherwise mentioned.
5
6

7 **Quantitative Analysis of the Reaction Kinetics Involved in the Formation of the Core-**
8 **Shell Octahedra.** The reduction rates of the Pd(II) and Pt(II) precursors were experimentally
9 measured by analyzing the concentrations of the precursors remaining in the reaction solution after
10 different periods of time. Such an analysis can be readily done with the assistance of an inductively
11 coupled plasma mass spectrometer (ICP-MS, NexION 300Q, PerkinElmer). In a typical protocol,
12 we started the timer upon immersing the reaction container into an oil bath set to 160 °C. Using
13 glass pipets, we constantly sampled aliquots of about 0.2 mL from the reaction solution at different
14 points. The aliquots were quickly injected into 0.8 mL of aqueous KBr solution (500 mg mL⁻¹)
15 kept at 0 °C to terminate the reduction. We then centrifuged the solution at 55000 rpm for 60 min
16 to remove all the nanoparticles while keeping the Pd(II) and Pt(II) precursors in the supernatant.
17 Prior to ICP-MS analysis, the supernatant was collected and diluted with 1% (v/v) aqueous HNO₃
18 solution to reach an ion concentration of about 100 ppb. From the ICP-MS data, we derived the
19 rate constant (*k*) by performing a linear fit to the plot of ln[Pd(II)] or ln[Pt(II)] *vs.* the reaction time.
20 Once the rate constant was known, the instantaneous concentrations of remaining Pd(II) or Pt(II)
21 precursor could be calculated as a function of reaction time, if the reaction temperature is fixed.
22
23

24 **Instrumentation.** We took all transmission electron microscopy (TEM) images on a Hitachi
25 HT7700 (Hitachi, Tokyo, Japan) at an operation voltage of 120 kV. High-resolution high-angle
26 annular dark-field scanning transmission electron microscopy (HAADF-STEM) and tomography
27 images were captured on a JEOL JEM 2200FS STEM/TEM microscope equipped with a CEOS
28 probe corrector (Heidelberg, Germany). Energy-dispersive X-ray (EDX) analysis was performed
29 in the STEM mode on an aberration-corrected JEOL 2200FS electron microscope equipped with
30 a Bruker-AXS SDD detector. The metal content, including the concentration of metal ions, in a
31 sample was measured using ICP-MS analysis.
32
33

34 **Preparation of the Working Electrodes.** Firstly, we loaded the as-prepared Pd@Pt_{IL} core-
35 shell octahedra on a carbon support (Ketjen Black EC-300J) at a metal content of 20% in terms of
36 the total mass of Pd and Pt (based on ICP-MS analysis). Typically, we dispersed 2 mg of the
37 Pd@Pt_{IL} core-shell octahedra and 8 mg of Ketjen black in 8 mL of ethanol under ultrasonication
38 for about 4 h. We then collected the carbon-supported Pd@Pt_{IL} octahedra using centrifugation, re-
39 dispersed them in 10 mL of acetic acid, and heated the mixture at 60 °C for 10 h to help remove
40
41
42
43
44
45

1
2
3 chemical species adsorbed on the surface of the metal particles. Finally, the catalyst was collected
4 through centrifugation and washed six times with ethanol. Once dried in an oven, we re-dispersed
5 3 mg of the catalyst in a mixture of 1 mL of isopropanol, 1 mL of DI water, and 40 μ L of 5%
6 Nafion under ultrasonication for about 60 min. We then placed 10 μ L of the suspension on a pre-
7 cleaned glassy carbon rotating disk electrode (RDE, Pine Research Instrumentation) and dried the
8 sample under ambient conditions. The RDE had a geometric area of 0.196 cm^2 . We used the Pt/C
9 catalyst from Tanaka Kinkinzoku Kogyo (TKK) as a benchmark for comparison. This state-of-
10 the-art catalyst contained 46.1 wt % 2.8 nm Pt nanoparticles supported on Ketjen Black EC-300J.
11 We dispersed 2 mg of the Pt/C catalyst in a mixture of 1 mL of isopropanol, 1 mL of DI water,
12 and 40 μ L of 5% Nafion under ultrasonication for about 60 min to produce an ink. We then placed
13 10 μ L of the ink on a pre-cleaned glassy carbon RDE and let the sample dry under ambient
14 conditions.
15
16

17 **Electrochemical Measurements.** We conducted all the electrochemical measurements
18 using a glassy carbon RDE connected to a CHI 600E potentiostat (CH Instruments). We used
19 Hydroflex hydrogen reference electrode (Gaskatel) and a Pt mesh as the reference and counter
20 electrodes, respectively. Typically, all potentials were converted potentials to values in reference
21 to reversible hydrogen electrode (RHE), or V_{RHE} . The 0.1 M HClO_4 electrolyte was prepared by
22 diluting a 70% stock solution with DI water, with the CV curve being recorded at room temperature
23 in a N_2 -saturated 0.1 M HClO_4 solution in the potential range of 0.08–1.10 V_{RHE} at a scanning rate
24 of 50 mV s^{-1} . We derived the specific electrochemical active surface area (ECSA) of each catalyst
25 from the average charges associated with hydrogen adsorption and desorption in the region of
26 0.08–0.43 V_{RHE} by taking a reference value of 240 $\mu\text{C cm}^{-2}$ (for $\text{Pd}@\text{Pt}_{1\text{L}}$ octahedra) for the
27 complete desorption of a monolayer of hydrogen from Pt(111) surface. The ORR activity of each
28 catalyst was measured in an O_2 -saturated 0.1 M HClO_4 solution at room temperature in the
29 potential range of 0.08–1.10 V_{RHE} , typically at a scanning rate of 10 mV s^{-1} and a rotating speed
30 of 1600 rpm. We corrected the ORR data using ohmic iR drop compensation. For the accelerated
31 durability test, CVs and ORR polarization curves were recorded after sweeping the catalyst in an
32 O_2 -saturated 0.1 M HClO_4 solution at room temperature for 5000, and 10,000 cycles in the range
33 of 0.6 and 1.1 V_{RHE} at a rate of 0.1 V s^{-1} .
34
35

36 **DFT Calculations.** We performed planewave density functional theory (DFT) calculations
37 employing the projector augmented wave (PAW) potentials^{29,30} and the GGA-PW91 exchange
38

correlation functional,³¹ as realized in the Vienna *ab initio* simulation package (VASP).^{32,33} We expanded the Kohn-Sham electron wave function in a plane wave basis set with a kinetic energy cutoff of 400 eV. The lattice constant of bulk Pd was calculated to be 3.96 Å, in agreement with the experimental value of 3.89 Å.³⁴

Metal Atom Diffusion on Edge Model. Similar to our recent work,³⁵ we created an edge model by symmetrically eliminating a total of 40 atoms out of the top layers of an eight-layer Pd(110) slab of a 5×4 unit cell, to expose two adjacent {111} facets on either side of the edge. We then removed the edge atoms to expose the {110} facet at the interface between the two {111} planes, as shown in Figure S3. Therefore, this model is an accurate representation of the edges of the as-synthesized nanocrystals, as depicted in Figure 5A. The bottom two layers were fixed at their bulk positions, while the remainder of the atoms were allowed to fully relax. A Monkhorst-Pack *k*-point mesh of 1×2×1 was used to sample the Brillouin zone.³⁶ Activation energy barriers of diffusion of Pt atoms on the Pd edge model were calculated using the climbing-image nudged elastic band (CI-NEB) method,³⁷ with seven intermediate images interpolated between the initial and final states. Each image was converged to less than 0.10 eV/Å calculated force on all atoms.

Slab Calculations and Surface Segregation. To model ORR on octahedral nanocrystals, we performed calculations for the adsorption of O and OH on periodic (2×2) unit cells, representing a coverage of 0.25 ML. All slabs exposed the {111} facet and were 5 atomic-layers thick, with the bottom two layers fixed, and the remainder of the atoms (including the adsorbates) allowed to fully relax. Approximately, vacuum of 14 Å thick was used to separate the vertical images of the slab to avoid unphysical interactions in the *z*-direction. Adsorption was only allowed for the top surface of the slabs, with the inclusion of appropriate dipole correction to the electrostatic potential.^{38,39} To capture small differences in energetics, we sampled the Brillouin zone using a dense Monkhorst-Pack *k*-point mesh of 10×10×1,³⁶ and converged geometric optimizations to 0.01 eV/Å Hellmann-Feynman interatomic forces. We performed these calculations on slabs representing Pd and Pd@Pt_{IL} core-shell in which the atoms of the top atomic layer of the Pd slab were replaced with Pt atoms.

As revealed by the EDX line scans for the Pd@Pt_{IL} octahedral nanocrystals, a mixed Pd-Pt composition might be possible for the surface layers. Therefore, we permuted the Pt atoms among the top two layers to yield top layer compositions of 0%, 25%, 50%, 75%, and 100% of Pt atoms for the slab models representing the Pd@Pt_{IL} core-shell octahedra, with the remaining Pt atoms

located in the immediate subsurface layer. All these different $\text{Pd}@\text{Pt}_{\text{IL}}$ core-shell slab models are designed at the lattice constant of Pd, given that Pt is the minority species. In Table S1, we compare the total energies of these different slab configurations in vacuum, and in the presence of 0.25 ML coverage of O or OH. Consistent with literature,⁴⁰ we have found that Pt prefers to occupy the subsurface in vacuum, giving a 0% Pt composition for the top layer in the absence of any adsorbates, (see Table S1). On the other hand, O and OH were both found to prefer a mixed surface layer composition; specifically, of 50% Pt under 0.25 ML of O, and 25% Pt under 0.25 ML of OH. In the cases of mixed compositions of the surface layer, O and OH were directly adsorbed to the Pt atom(s).

Calculations of ORR Activities on Slab Models. Gibbs free energies of gas-phase species (*i.e.*, H_2O) and surface species (*i.e.*, O and OH) were calculated as $G = E + \text{ZPE} - TS$, where E is the total electronic energy, ZPE is the zero-point energy, T is the absolute temperature of 298.15 K, and S is entropy. Both S and ZPE were estimated from the translational, vibrational, and rotational modes in the context of vibrational frequency calculations. The vibrational frequencies were estimated through numerical (*i.e.*, finite difference approximation) second-order differentiation of forces with a step size of 0.015 Å, within the framework of harmonic oscillator approximation. To take into account the applied bias in electrochemical measurements, we employed the computational reversible hydrogen electrode approach of Nørskov and coworkers.⁴¹ The reference electrode for this approach is the reversible hydrogen electrode (RHE), at which protons and electrons are in thermodynamic equilibrium with hydrogen gas at a defined potential of 0.0 V, all pH, and standard conditions of temperature (298.15 K) and pressure (1 atm). Therefore, by definition, $\Delta G = 0.00$ for $\frac{1}{2} \text{H}_2(\text{g}) \leftrightarrow \text{H}^+ + \text{e}^-$ at 0.0 V_{RHE}. This means that the free energy of a proton-electron pair equals half that of hydrogen gas ($\text{H}_2(\text{g})$) as calculated by DFT, at 0.0 V_{RHE}. To modify the free energy in response to applied electrochemical bias (U), the free energy change of an electron is calculated as $-\lvert e \rvert U$, where $\lvert e \rvert$ is the absolute charge of an electron. In sum, the free energy change of either of our electrochemical steps ($\text{O} + \text{H}^+ + \text{e}^- \rightarrow \text{OH}$, and $\text{OH} + \text{H}^+ + \text{e}^- \rightarrow \text{H}_2\text{O}(\text{g})$) is calculated as $\Delta G = \Delta E + \Delta \text{ZPE} - T\Delta S + \lvert e \rvert U$. Therefore, both electrochemical steps become more endothermic at more positive potentials (or bias). Given that we did not include a water bilayer in our model for computational convenience, we stabilized the free energy of adsorbed OH by 0.50 eV, while no stabilization was considered for adsorbed O, consistent with literature.⁴²

Calculations of the Mechanism of Surface Segregation. To rationalize the activity loss during the accelerated durability test, and given the thermodynamic propensity of Pd to at least partially segregate to the top metal layer (see Table S1), we performed a detailed study of the mechanism by which a surface Pt atom can swap positions with a Pd atom in the immediate subsurface layer. Specifically, we performed such a study for slabs in vacuum, and in the presence of 0.25 ML of O or OH. Furthermore, we calculated the swapping activation energy barriers (calculated *via* CI-NEB) up to a surface composition of 75% Pd,³⁷ given that O and OH are destabilized on pure Pd surface layers (Table S1). We have found that four-body rotations (which involves two top-layer metal atoms and two subsurface metal atoms) are less energetically favorable, and therefore we only report the activation energy barriers of three body rotations. We typically found multiple local minima along the trajectory of the minimum energy path (MEP) for this mechanism. In such cases, the MEP was broken down to intermediate pieces connecting the initial state, final state, and all local minima in between. The reported E_a is that of the most difficult intermediate piece of the MEP, while the reported ΔE is simply the difference in total energy of the final state and the initial state.

RESULTS AND DISCUSSION

In a standard batch synthesis of the Pd@Pt_{1L} core-shell octahedra, Na₂PdCl₄ and Pt(acac)₂ were co-dissolved in EG and then added into another solution of PVP and AA in EG at room temperature through the use of a pipet. After the reaction had been continued at 160 °C for 3 h, we obtained the core-shell octahedra. Figure 1, A and B, shows transmission electron microscopy (TEM) and high-angle annular dark-field scanning transmission electron microscopy (HAADF-STEM) images of the as-synthesized core-shell octahedra with an average edge length of 6.7±0.4 nm, together with good uniformity in terms of both size and shape. Figure 1, C and D, shows bright-field and atomic-resolution HAADF-STEM images taken from an individual octahedron. These images indicate that the nanocrystals were dominated by {111} facets on the side faces, together with much smaller {100} facets at the slightly truncated corners. The large difference in atomic number between the two elements involved led to contrast between the Pt shell and the Pd core. More importantly, these images suggest that the Pt shell only had a thickness of about one atomic layer. We also used ICP-MS to analyze the average number of Pt atomic layers in each core-shell nanocrystal and obtained a value of 0.95. Unless otherwise specified, we exclusively

use the data derived from ICP-MS in the following discussion because this number reflects the average value for a large number of particles. We also confirmed the formation of a core-shell structure by analyzing the nanocrystal through the use of energy-dispersive X-ray spectroscopy (EDX) mapping (Figure 1E). According to ICP-MS analysis, the Pd/Pt molar ratio was 3.53 for the Pd@Pt_{IL} core-shell octahedra, which was almost identical to the value of 3.42 derived from the molar feeding ratio set for the Pd(II) and Pt(II) precursors. This result suggests that the conversion of both the Pd(II) and Pt(II) precursors could reach a level of >97% when both AA and EG were employed as the reductants.²⁵ Figure 1F shows the EDX line scans across an individual octahedron, confirming that Pt and Pd were mostly detected from the shell and core regions of the nanocrystal, respectively.

In order to elucidate how the core-shell octahedra were formed in our system, we analyzed the products sampled at different stages of a batch synthesis by TEM and ICP-MS. In this case, aliquots were taken out from the reaction mixture at different time points of a standard synthesis. Figure 2, A–D, shows TEM images of the nanocrystals obtained at different intervals after the reaction container had been immersed in the oil bath held at 160 °C. At $t = 2$ min, truncated octahedral nanocrystals with an average edge length of 6.0 ± 0.4 nm were formed (Figure 2A). After another 18 min, the nanocrystals had been transformed into an octahedral shape (Figure 2B). This result suggests that the growth largely occurred along the <100> directions in the initial stage of a synthesis because {100} facets have a high surface free energy than that of {111} facets. Once the nanocrystals had evolved into an octahedral shape largely encased by {111} facets, the shape tended to stay as the reaction time was prolonged. As shown in Figure 2, C and D, the edge length gradually increased from 6.2 ± 0.3 nm at $t = 20$ min to 6.5 ± 0.2 and 6.7 ± 0.4 nm for $t = 60$ and 120 min, respectively.

We further measured the changes in Pt/Pd atomic ratio during the synthesis by ICP-MS. As shown in Figure 3, the Pt/Pd ratio was only 0.03 for the products obtained at $t = 2$ min, suggesting that only the Pd(II) precursor had been reduced to form Pd truncated octahedral seeds. Afterwards, the Pt/Pd ratio of the resultant products increased to 0.55 as the reaction time was increased to 180 min. Both the electron microscopy images and ICP-MS results clearly confirm that the core-shell nanocrystals are sequentially formed through the formation of Pd core first, followed by the deposition of Pt overlayer. In a control experiment, only Pd truncated octahedra were observed when no Pt(II) precursor was added into a standard synthesis (Figure S4A). This result was also

1
2
3 consistent with the products obtained in Figure 2A. In this case, $\text{Pd}@\text{Pt}_{\text{IL}}$ core-shell octahedra
4 could still be formed when we introduced the $\text{Pt}(\text{acac})_2$ precursor into the reaction system at $t = 1$
5 h after almost all the $\text{Pd}(\text{II})$ precursor had been reduced (Figure S4B). These observations support
6 our anticipation that PdCl_4^{2-} was reduced at a much faster rate than $\text{Pt}(\text{acac})_2$ under the same
7 conditions. This difference in reduction rate can be largely attributed to the stronger complexation
8 between the acetylacetone ligand and Pt^{2+} and thereby a lower reduction potential.^{26,27} Taken
9 together, we can conclude that the core-shell nanocrystals were formed through the initial
10 nucleation and growth of Pd octahedral nanocrystals, which then served as seeds for the deposition
11 of Pt overlayers.
12
13

14 We believe that the temporal separation between the reduction of $\text{Pd}(\text{II})$ and $\text{Pt}(\text{II})$ precursors,
15 due to the large difference in reduction kinetics, is a key factor in promoting the formation of a
16 core-shell structure. To gain insights into the reduction kinetics of a synthesis, we analyzed the
17 percentage of metal ions remaining in the reaction solution as a function of reaction time using
18 ICP-MS and then derived the rate law. In general, the reduction of a salt precursor should follow
19 the second-order rate law owing to the requirement of collision and then electron transfer between
20 the precursor and reductant species.⁴³ In the present work, the amount of the reductant was used
21 in large excess relative to that of the precursor, so the concentration of the reductant was supposed
22 to change very little during the entire synthesis. As a result, it is no unreasonable to approximate
23 the reduction kinetics as a pseudo-first-order reaction. Figure 4, A and B, shows plots of $\ln[\text{Pt}(\text{II})]$
24 and $\ln[\text{Pd}(\text{II})]$ as a function of reaction time for the standard synthesis conducted at 160 °C. As
25 expected, the values of $\ln[\text{Pt}(\text{II})]$, and $\ln[\text{Pd}(\text{II})]$, indeed decreased linearly with the reaction time,
26 confirming that the reduction was first-order with respect to the precursor concentration. From the
27 slopes of the linear regression lines, we obtained rate constants of 6.4×10^{-4} and $1.8 \times 10^{-2} \text{ s}^{-1}$ for
28 the $\text{Pt}(\text{II})$ and $\text{Pd}(\text{II})$ precursors, respectively, when the reduction was performed by a mixture of
29 EG and AA. We repeated the kinetic measurement two more times to obtain the average reduction
30 rate constants. We obtained 6.40×10^{-4} , 6.42×10^{-4} , and $6.38 \times 10^{-4} \text{ s}^{-1}$ in rate constant for the $\text{Pt}(\text{II})$
31 precursor, which gave a standard deviation of 1.60×10^{-6} . Similarly, the standard deviation for the
32 rate constant of the $\text{Pd}(\text{II})$ precursor was determined to be 1.29×10^{-4} . From these data, it can be
33 concluded that the measurements were reasonably accurate. The ratio between the rate constants
34 for the $\text{Pt}(\text{II})$ and $\text{Pd}(\text{II})$ precursors was only 0.036. Combined with the initial concentration of
35 $\text{Pt}(\text{II})$ ($3.80 \times 10^{-3} \text{ M}$) and $\text{Pd}(\text{II})$ ($1.30 \times 10^{-2} \text{ M}$), the corresponding initial reduction rate of the $\text{Pt}(\text{II})$
36

1
2
3 precursor (2.40×10^{-6} M s⁻¹) was estimated to be almost two orders of magnitude (1:98) slower
4 than that of the Pd(II) precursor (2.34×10^{-4} M s⁻¹). Taken together, it can be concluded that it is
5 the drastic difference in initial reduction rate that led to the formation of a core-shell structure.
6 This study offers another example to qualitatively demonstrate that the structure of the products
7 can be controlled by manipulating the reduction kinetics, especially the initial reduction rate.
8
9

10 Figure 5A schematically illustrates our proposed mechanism to account for the formation of
11 the Pd@Pt_{IL} core-shell octahedra. Upon heating to 160 °C, the strong reducing power associated
12 with the mixture of AA and EG can quickly reduce the Pd(II) precursor to the elemental form.
13 According to the mechanism proposed by LaMer and co-workers, the Pd atoms will start to
14 aggregate to generate small clusters (*i.e.*, nuclei) through a homogeneous nucleation process once
15 their concentration has reached the level of supersaturation.⁴⁴ Afterwards, the nuclei will grow into
16 Pd nanocrystals with increasingly enlarged sizes until the precursor has been depleted. According
17 to the result from a previous study,⁴⁵ an initial reduction rate around 2.34×10^{-4} M s⁻¹ should lead
18 to the formation of single-crystal seeds, typically in the form of truncated octahedra (or the so-
19 called Wulff polyhedra) encased by a mix of {111} and {100} facets. Because the truncated
20 octahedron has a nearly spherical shape and thus the smallest ratio between the surface area and
21 volume, the total surface free energy will be minimized.⁴⁶ This result is supported by the shape
22 and composition evolution processes shown in Figure 2A and Figure 3. In contrast to the Pd(II)
23 precursor, the Pt(II) precursor was reduced at a much slower rate under the same experimental
24 conditions because of the strong complexation between Pt²⁺ and acetylacetone ligand. As the Pt(II)
25 precursor was gradually reduced, the Pt atoms were deposited on the edges of the Pd core owing
26 to a small lattice mismatch of 0.77% between Pt and Pd, as well as the lower coordination numbers
27 at the edges.^{10,47} In particular, the growth mainly occurred along the <110> directions in the initial
28 stage of a synthesis because the surface energy of {110} facets are greater than that of {111}
29 ones.^{47,48} Afterwards, the deposited Pt atoms diffused to side faces and corners at the elevated
30 temperature, leading to the production of Pd@Pt_{IL} core-shell octahedra.
31
32
33
34
35
36
37
38
39
40
41
42
43
44
45
46
47

48 To further understand the mechanism responsible for the formation of a core-shell structure,
49 we performed a detailed DFT study of the diffusion of Pt and Pd atoms on an edge model, in which
50 two {111} terraces are joined with a {110} edge, see Figure S3. This study is summarized in Figure
51 5, B–E and Table 1. We calculated the surface energy of the three Pd facets and found that their
52 order went by Pd{110} > Pd{100} > Pd{111}. Given that Pd{110} has the highest surface energy
53
54
55
56
57
58
59
60

1
2
3 among the three facets, the {110} edges should represent a preferable landing spot for the Pt atoms
4 from solution. Therefore, we start with a Pt atom deposited on a {110} hollow site on the edge of
5 the Pd seed, see Figure 5B. There are a few possible diffusion paths for the Pt atom to follow; the
6 easiest is the diffusion of the Pt atom along the edge (path 1 in Figure 5B), with an activation
7 energy barrier of 0.57 eV. To escape this edge, however, the Pt atom has to hop over the
8 surrounding Pd atoms onto the adjacent terrace (path 2), or substitute one of the surrounding Pd
9 atoms while pushing the Pd atom onto the terrace (substitution; path 3). While hopping (path 2) is
10 highly activated with 1.59 eV activation energy barrier, substitution (path 3) has an activation
11 energy barrier of only 0.66 eV. Furthermore, substitution is 0.46 eV less endothermic than the
12 hopping mechanism. Together, these quantities confirm that substitution will be the decisive
13 mechanism for diffusion from edges to terraces. The diffusion of the displaced Pd atom across the
14 terrace, and away from the edge, proceeds easily with barriers below 0.30 eV (paths 4-6 in Figure
15 5C and Table 1). Assuming that this displaced Pd atom has diffused away from the edge, we
16 deposit a second Pt atom on a {110} hollow site, see Figure 5D. We already know that hopping to
17 the terrace is not competitive, and therefore, the question as to the preferred diffusion path of the
18 newly-deposited Pt atom becomes whether such Pt atom would rather displace a Pt or a Pd atom
19 from the edge to the terrace, as conveyed by paths 7 and 8, respectively. We find that path 8 is less
20 endothermic than path 7 by 0.30 eV, and has an activation energy barrier of 0.82 eV; that is, 0.26
21 eV lower than path 7. Therefore, a newly-deposited Pt atom would rather displace a Pd atom to
22 occupy its position and sit next to another Pt atom on the edge. This process is repeated again in
23 Figure 5E (assuming that the displaced Pd atom has diffused away from the edge), and similarly,
24 we calculate that Pt would substitute a Pd atom (path 10) instead of another Pt atom (path 9). These
25 results strongly suggest that the as-synthesized $\text{Pd}@\text{Pt}_{\text{IL}}$ core-shell octahedra should have a
26 slightly mixed surface composition. At later stages of the synthesis, the newly-deposited Pt atoms
27 will only find Pt atoms at the edge to substitute, thus finally coating the seed terraces with a Pt
28 overlayer. Like Pd, Pt atom hopping across the terraces away from the edges is expected to be very
29 easy (calculated activation energy barriers – assuming pure Pd seeds – are less than 0.20 eV).
30 Finally, it is worth noting that all activation energy barriers tabulated in Table 1 are surmountable
31 at the synthesis temperature of 160 °C. A slightly mixed surface composition for the as-synthesized
32 $\text{Pd}@\text{Pt}_{\text{IL}}$ core-shell octahedra is also supported by the EDX line scans of Figure 1F.
33
34
35
36
37
38
39
40
41
42
43
44
45
46
47
48
49
50
51
52
53
54
55
56
57
58
59
60

We used the rotating disk electrode (RDE) method to characterize the ORR performance of the catalyst based on the $\text{Pd}@\text{Pt}_{\text{IL}}$ core-shell octahedra (synthesized in a continuous flow reactor), with a commercial Pt/C catalyst serving as a reference. Prior to electrochemical measurements, the core-shell octahedra were deposited on a carbon support to obtain a $\text{Pd}@\text{Pt}_{\text{IL}}/\text{C}$ catalyst (Figure S5). Through ICP-MS analysis, we confirmed that the Pd/Pt molar ratio for the $\text{Pd}@\text{Pt}_{\text{IL}}/\text{C}$ catalyst was almost identical to the value of the $\text{Pd}@\text{Pt}_{\text{IL}}$ octahedra before acid treatment (3.52 vs. 3.53). The TEM and ICP-MS results suggest that both the shape and composition of the $\text{Pd}@\text{Pt}_{\text{IL}}/\text{C}$ catalyst were maintained during the treatment with acetic acid. Figure 6A compares the cyclic voltammograms (CVs) recorded from the $\text{Pd}@\text{Pt}_{\text{IL}}/\text{C}$ and Pt/C catalysts, respectively, in the potential range of 0.08–1.10 V, relative to the reversible hydrogen electrode (V_{RHE}). From the average charges associated with hydrogen adsorption and desorption in the range of 0.08–0.43 V, the electrochemical active surface areas (ECSAs) of these two catalysts were obtained and then normalized to the amounts of Pt in the samples, generating specific ECSAs. Although the $\text{Pd}@\text{Pt}_{\text{IL}}$ octahedra had an overall size more than twice greater than that of the Pt nanoparticles in the Pt/C, the specific ECSA of the $\text{Pd}@\text{Pt}_{\text{IL}}/\text{C}$ was on par with that of the Pt/C ($74.3 \text{ m}^2 \text{ g}^{-1} \text{ Pt}$ vs. $79.6 \text{ m}^2 \text{ g}^{-1} \text{ Pt}$). These results confirm that the utilization efficiency of Pt atoms could indeed be increased by depositing them as an ultrathin shell on Pd nanocrystals.

Figure 6B shows the positive-going ORR polarization curves recorded from the two catalysts, from which we could derive the kinetic currents using the Koutecky–Levich equation and then normalize the values to the ECSA and Pt (or Pt+Pd) mass, respectively, to obtain the specific and mass activities (*i.e.*, $j_{\text{k,specific}}$ and $j_{\text{k,mass}}$). The results are plotted in Figure S6, A and B. As expected, both the specific and mass activities of the $\text{Pd}@\text{Pt}_{\text{IL}}/\text{C}$ catalyst were enhanced in comparison with those of the commercial Pt/C in the potential region of 0.86–0.94 V. Specifically, the specific activity (1.01 mA cm^{-2}) of the $\text{Pd}@\text{Pt}_{\text{IL}}/\text{C}$ catalyst at 0.9 V_{RHE} showed an enhancement of almost three folds when benchmarked against the Pt/C (0.35 mA cm^{-2}). We believe that the enhancement in specific activity mainly comes from the ligand effect, in addition to the compressive strain arising from the lattice mismatch between Pt and Pd.^{19,49–51} At 0.9 V_{RHE} , the mass activity of the $\text{Pd}@\text{Pt}_{\text{IL}}/\text{C}$ catalyst was about $0.75 \text{ A mg}^{-1} \text{ Pt}$, almost three times as high as that of the Pt/C ($0.28 \text{ A mg}^{-1} \text{ Pt}$). In this case, the enhancement in mass activity should directly come from the extremely high utilization efficiency of Pt atoms for the $\text{Pd}@\text{Pt}_{\text{IL}}$ octahedral nanocrystals.

1
2
3 As shown in Figure 6, C and D, the $\text{Pd}@\text{Pt}_{\text{IL}}/\text{C}$ catalyst also exhibited excellent durability.
4 The specific ECSA of the $\text{Pd}@\text{Pt}_{\text{IL}}/\text{C}$ catalyst dropped less than 12% after 5,000 cycles of
5 accelerated durability tests at room temperature. In comparison, the specific ECSA of the Pt/C
6 catalyst decreased by almost 30%. Even after 10,000 cycles, the specific ECSA of the $\text{Pd}@\text{Pt}_{\text{IL}}/\text{C}$
7 catalyst was retained at 72% of its original value while the specific ECSA of the Pt/C catalyst only
8 held 58% of its initial value. More specifically, $\text{Pd}@\text{Pt}_{\text{IL}}/\text{C}$ catalyst still had a mass activity of 0.56
9 $\text{A mg}^{-1} \text{pt}$ after 5,000 cycles of durability test. After 10,000 cycles, the mass activity showed a
10 slight drop to become $0.45 \text{ A mg}^{-1} \text{pt}$. Remarkably, this value was still about twice that of the mass
11 activity of the Pt/C in the pristine state. According to a recent report, Pt atoms could be oxidized
12 and dissolved from the Pt counter electrode, and then re-deposited on the working electrode during
13 the electrocatalytic process.⁵² As a result, additional Pt nanoparticles are expected to form on the
14 carbon support during the durability test. Based on the TEM images shown in Figure S5 and Figure
15 S7, however, no additional Pt nanoparticles was observed on the carbon support for the $\text{Pd}@\text{Pt}_{\text{IL}}$
16 octahedra after the durability test. In this case, the number of Pt atoms dissolved from the counter
17 electrode might be too little to nucleate and then grow into a separate population of observable
18 nanoparticles. Alternatively, the small number of Pt atoms from the counter electrode should favor
19 deposition on the existing $\text{Pd}@\text{Pt}_{\text{IL}}$ octahedra. However, because of the shape transformation
20 during the durability test (see below), it was challenging to clearly resolve the possible deposition
21 of additional Pt atoms onto the $\text{Pd}@\text{Pt}_{\text{IL}}$ octahedra.
22
23

24 During the durability test, some of the $\text{Pd}@\text{Pt}_{\text{IL}}$ octahedra were found to evolve into spherical
25 particles with a diameter in the range of 5–6 nm instead of generating a cage-like structure (Figure
26 S7). This result is somewhat different from what was reported for $\text{Pd}@\text{Pt}$ core-shell nanocrystals
27 in literature.¹⁴ We believe the difference can be largely attributed to the disparity in particle size.
28 The $\text{Pd}@\text{Pt}_{\text{nL}}$ ($n \geq 2$) octahedral nanocrystals reported in our early work were larger than 15 nm in
29 size.¹⁴ In contrast, the overall size of the $\text{Pd}@\text{Pt}_{\text{IL}}$ octahedral nanocrystals reported in the present
30 work was much smaller, around 6 nm. As such, when the Pd cores were selectively dissolved and
31 leached out during the repeated cycles, the remaining Pt atoms tended to migrate for the formation
32 of solid, spherical particles in an effort to reduce the total energy of the system. This argument is
33 consistent with what was reported in literature.⁹ Due to the selective dissolution of Pd atoms from
34 the core, the proportion of {111} facets on the particle's surface dropped and the size slightly
35
36

decreased relative to the sample before durability test. As a result, both the specific ECSA and mass activity decreased.

We seek here to rationalize the high stability of the Pd@Pt_{IL} octahedra. The calculated minimum energy adsorption configurations of O and OH on Pd@Pt_{IL} core-shell octahedra slab models are given in Table S1, while the free energies of protonation of O and OH on all surfaces studied are given in Table S2. Despite the propensity of Pt to segregate to the subsurface layer in vacuum, O and OH are most stabilized on a mixed-composition surface layer model (50% Pt and 25% Pt for 0.25 ML of O and OH, respectively) in which O and OH are coordinated to the surface Pt atom(s), as shown in the insets of Table S1. However, a significantly mixed Pd-Pt layer (as suggested by the thermodynamics of adsorption of O and OH) should offer a deteriorated performance for ORR, as indicated by higher calculated free energies of protonation on such surfaces compared to a pure Pt layer (Table S2). We note, however, that often such compositional transformations are controlled by kinetics rather than thermodynamics. To prove this point, we calculated the activation energy barriers for Pd-Pt atom exchange at the interface between the Pd body and the top layer in our slab models, up to 25% Pt composition of top surface layer. Too high barriers for these swapping processes would explain the durability of the Pd@Pt_{IL} octahedra. The results are given in Table S3 for slabs under vacuum, and 0.25 ML of either O or OH. The activation energy barriers are indeed very high (>2 eV for most cases) for all systems studied. We further repeated this study, albeit in the presence of a single subsurface vacancy, in which one Pd atom was omitted from the first subsurface layer. We have previously shown that Pd octahedra are seeded during synthesis with a significant density of subsurface vacancies,³⁵ and these vacancies could only proliferate at prolonged dissolution of Pd. The calculated activation energy barriers tabulated in Table S4 for this scenario are smaller than those for the case where there were no subsurface vacancies, but are not small enough to readily occur at room temperature. This trend indicates that activation energy barriers could fall even lower in the presence of a bigger ensemble of subsurface vacancies, which is possible with the continuous dissolution of Pd at prolonged operation, thus bringing down the ORR activity. We note that this Pd dissolution process is readily initiated, given the slightly mixed top layer composition, as described earlier. Nevertheless, the high barriers reported in this study indicate that significant Pd-Pt swapping among the top two layers cannot occur on a wide scale, thus explaining the durability of the Pd@Pt_{IL} octahedra.

CONCLUSIONS

In summary, we have demonstrated a facile protocol for the one-pot synthesis of Pd@Pt core-shell octahedra with ultrathin skins that are only one atomic layer in thickness. Our kinetic analysis suggests that the formation of such a core-shell structure in one pot is mainly enabled by the large difference between the initial reduction rates of the Pd(II) and Pt(II) precursors involved in the synthesis. Specifically, the Pd(II) precursor is reduced in the initial stage to generate Pd truncated octahedra, followed by the reduction of the Pt(II) precursor for the deposition of Pt atoms as an ultrathin shell on each Pd nanocrystal. Our electrochemical measurements demonstrate that the Pd@Pt_{1L} octahedral nanocrystals have greatly enhanced activity and durability toward ORR when compared with a state-of-the-art Pt/C catalyst. After 10,000 cycles of accelerated durability tests, the Pd@Pt_{1L} octahedral nanocrystals still have a mass activity of about twice that of the pristine Pt/C catalyst. More importantly, we have also demonstrated the use of continuous flow reactors for potentially scaling up the production of the core-shell nanocrystals in large quality and with good uniformity. The success of this synthesis demonstrates that one can manipulate the reaction kinetics of the precursors to develop bimetallic nanocrystals with enhanced performance toward ORR and other reactions. This strategy can be potentially extended to other metals and even other types of inorganic materials. Our DFT calculations also offer atomic scale explanations of experimentally-observed behaviors at three different occasions: 1) the synthesis results in a slightly mixed surface layer composition due to the preference of deposited Pt atoms to substitute Pd at the edges, 2) more extensive Pt-Pd mixing of the surface layer is thermodynamically preferred, but results in deteriorated ORR activities, thus explaining the fundamental reason behind loss of activity at prolonged operation, and 3) the calculated activation energy barriers for Pd-Pt swapping to enrich the surface layer with more Pd are prohibitive, thus indicating that such processes will be limited, and in turn, rationalizing the high stability of the Pd@Pt_{1L} octahedra. The extensive insights gained through DFT indicate the promise of combining precise synthesis, accurate characterization and kinetic measurements, with representative DFT models to gain an appreciation of the full picture of materials synthesis and catalysis, at the atomic scale.

ASSOCIATED CONTENT

Supporting Information

The Supporting Information is available free of charge *via* the Internet at <http://pubs.acs.org>. Photograph showing the setup used for the continuous synthesis of Pd@Pt_{1L} octahedra; TEM image of the Pd@Pt_{1L} octahedral nanocrystals synthesized in continuous flow reactors; Images of the edge model; TEM images of the Pd@Pt_{1L}/C octahedra catalysts; Plots of the specific and mass ORR activities; TEM image of the Pd@Pt_{1L}/C octahedra catalyst after accelerated durability test.

AUTHOR INFORMATION

Corresponding Authors

*E-mail: manos@engr.wisc.edu (computational work).

*E-mail: younan.xia@bme.gatech.edu (experimental work).

Notes

The authors declare no competing financial interest.

ACKNOWLEDGEMENTS

This work was supported in part by an NSF joint grant (CHE-1505441) to Georgia Tech and UW-Madison, an NSF grant (CMMI-1634687) to Georgia Tech, and startup funds from Georgia Tech. As visiting Ph.D. students from Chongqing University, and Donghua University, respectively. M.Z., and H.W. were also partially supported by the China Scholarship Council (CSC). Z.D.H. gratefully acknowledges support from the National Science Foundation Graduate Research Fellowship under Grant No. DGE-1148903 and the Georgia Tech-ORNL Fellowship. A portion of this research was completed at the Center for Nanophase Materials Sciences, which is a DOE Office of Science User Facility. Calculations were performed at supercomputing centers located at the Environmental Molecular Sciences Laboratory, which is sponsored by the DOE Office of Biological and Environmental Research at Pacific Northwest National Laboratory; the Center for Nanoscale Materials at Argonne National Laboratory, supported by DOE contract DE-AC02-06CH11357; and the National Energy Research Scientific Computing Center (NERSC), a DOE Office of Science User Facility supported by DOE contract DE-AC02-05CH11231; and the UW-Madison Center for High Throughput Computing (CHTC), supported by UW-Madison, the Advanced Computing Initiative, the Wisconsin Alumni Research Foundation, the Wisconsin Institutes for Discovery, and the National Science Foundation.

1
2
3
4
5 **REFERENCES**
6
7
8
9
10
11
12
13
14
15
16
17
18
19
20
21
22
23
24
25
26
27
28
29
30
31
32
33
34
35
36
37
38
39
40
41
42
43
44
45
46
47
48
49
50
51
52
53
54
55
56
57
58
59
60

(1) Debe, M. K. Electrocatalyst Approaches and Challenges for Automotive Fuel Cells. *Nature* **2012**, *486*, 43–51.

(2) Chen, J.; Lim, B.; Lee, E. P.; Xia, Y. Shape-Controlled Synthesis of Platinum Nanocrystals for Catalytic and Electrocatalytic Applications. *Nano Today* **2009**, *4*, 81–95.

(3) Stamenkovic, V. R.; Strmcnik, D.; Lopes, P. P.; Markovic, N. M. Energy and Fuels from Electrochemical Interfaces. *Nat. Mater.* **2017**, *16*, 57–69.

(4) Wang, Y.-J.; Wilkinson, D. P.; Zhang, J. Noncarbon Support Materials for Polymer Electrolyte Membrane Fuel Cell Electrocatalysts. *Chem. Rev.* **2011**, *111*, 7625–7651.

(5) Cui, C.; Gan, L.; Heggen, M.; Rudi, S.; Strasser, P. Compositional Segregation in Shaped Pt Alloy Nanoparticles and Their Structural Behaviour During Electrocatalysis. *Nat. Mater.* **2013**, *12*, 765–771.

(6) Choi, S.-I.; Xie, S.; Shao, M.; Odell, J. H.; Lu, N.; Peng, H.-C.; Protsailo, L.; Guerrero, S.; Park, J.; Xia, X.; Wang, J.; Kim, M. J.; Xia, Y. Synthesis and Characterization of 9 nm Pt–Ni Octahedra with a Record High Activity of 3.3 A/mg_{Pt} for the Oxygen Reduction Reaction. *Nano Lett.* **2013**, *13*, 3420–3425.

(7) Zhang, L.; Roling, L. T.; Wang, X.; Vara, M.; Chi, M.; Liu, J.; Choi, S.-I.; Park, J.; Herron, J. A.; Xie, Z.; Mavrikakis, M.; Xia, Y. Platinum-Based Nanocages with Subnanometer-Thick Walls and Well-Defined, Controllable Facets. *Science* **2015**, *349*, 412–416.

(8) Chen, C.; Kang, Y.; Huo, Z.; Zhu, Z.; Huang, W.; Xin, H. L.; Snyder, J. D.; Li, D.; Herron, J. A.; Mavrikakis, M.; Chi, M.; More, K. L.; Li, Y.; Markovic, N. M.; Somorjai, G. A.; Yang, P.; Stamenkovic, V. R. Highly Crystalline Multimetallic Nanoframes with Three-Dimensional Electrocatalytic Surfaces. *Science* **2014**, *343*, 1339–1343.

(9) Sasaki, K.; Naohara, H.; Choi, Y.; Cai, Y.; Chen, W.-F.; Liu, P.; Adzic, R. R. Highly Stable Pt Monolayer on PdAu Nanoparticle Electrocatalysts for the Oxygen Reduction Reaction. *Nat. Commun.* **2012**, *3*, 1115.

(10) Xie, S.; Choi, S.-I.; Lu, N.; Roling, L. T.; Herron, J. A.; Zhang, L.; Park, J.; Wang, J.; Kim, M. J.; Xie, Z.; Mavrikakis, M.; Xia, Y. Atomic Layer-by-Layer Deposition of Pt on Pd Nanocubes for Catalysts with Enhanced Activity and Durability toward Oxygen Reduction. *Nano Lett.* **2014**, *14*, 3570–3576.

(11) You, H.; Yang, S.; Ding, B.; Yang, H. Synthesis of Colloidal Metal and Metal Alloy Nanoparticles for Electrochemical Energy Applications. *Chem. Soc. Rev.* **2013**, *42*, 2880–2904.

(12) Zhang, J.; Mo, Y.; Vukmirovic, M. B.; Klie, R.; Sasaki, K.; Adzic, R. R. Platinum Monolayer Electrocatalysts for O₂ Reduction: Pt Monolayer on Pd(111) and on Carbon-Supported Pd Nanoparticles. *J. Phys. Chem. B* **2004**, *108*, 10955–10964.

(13) Guo, S.; Li, D.; Zhu, H.; Zhang, S.; Markovic, N. M.; Stamenkovic, V. R.; Sun, S. FePt and CoPt Nanowires as Efficient Catalysts for the Oxygen Reduction Reaction. *Angew. Chem., Int. Ed.* **2013**, *52*, 3465–3468.

(14) Park, J.; Zhang, L.; Choi, S.-I.; Roling, L. T.; Lu, N.; Herron, J. A.; Xie, S.; Wang, J.; Kim, M. J.; Mavrikakis, M.; Xia, Y. Atomic Layer-by-Layer Deposition of Platinum on Palladium Octahedra for Enhanced Catalysts toward the Oxygen Reduction Reaction. *ACS Nano* **2015**, *9*, 2635–2647.

(15) Adzic, R. R.; Zhang, J.; Sasaki, K.; Vukmirovic, M. B.; Shao, M.; Wang, J. X.; Nilekar, A. U.; Mavrikakis, M.; Valerio, J. A.; Uribe, F. Platinum Monolayer Fuel Cell Electrocatalysts. *Top. Catal.* **2007**, *46*, 249–262.

(16) Zhang, J.; Vukmirovic, M. B.; Xu, Y.; Mavrikakis, M.; Adzic, R. R. Controlling the Catalytic Activity of Platinum-Monolayer Electrocatalysts for Oxygen Reduction with Different Substrates. *Angew. Chem., Int. Ed.* **2005**, *44*, 2132–2135.

(17) Stamenkovic, V. R.; Fowler, B.; Mun, B. S.; Wang, G.; Ross, P. N.; Lucas, C. A.; Markovic, N. M. Improved Oxygen Reduction Activity on Pt₃Ni(111) via Increased Surface Site Availability. *Science* **2007**, *315*, 493–497.

(18) Stamenkovic, V. R.; Mun, B. S.; Arenz, M.; Mayrhofer, K. J. J.; Lucas, C. A.; Wang, G.; Ross, P. N.; Markovic, N. M. Trends in Electrocatalysis on Extended and Nanoscale Pt-Bimetallic Alloy Surfaces. *Nat. Mater.* **2007**, *6*, 241–247.

(19) Strasser, P.; Koh, S.; Anniyev, T.; Greeley, J.; More, K.; Yu, C.; Liu, Z.; Kaya, S.; Nordlund, D.; Ogasawara, H.; Toney, M. F.; Nilsson, A. Lattice-Strain Control of the Activity in Dealloyed Core-Shell Fuel Cell Catalysts. *Nat. Chem.* **2010**, *2*, 454–460.

(20) Hunt, S. T.; Milina, M.; Alba-Rubio, A. C.; Hendon, C. H.; Dumesic, J. A.; Román-Leshkov, Y. Self-Assembly of Noble Metal Monolayers on Transition Metal Carbide Nanoparticle Catalysts. *Science* **2016**, *352*, 974–978.

(21) Wang, X.; Figueroa-Cosme, L.; Yang, X.; Luo, M.; Liu, J.; Xie, Z.; Xia, Y. Pt-Based Icosahedral Nanocages: Using a Combination of {111} Facets, Twin Defects, and Ultrathin Walls to Greatly Enhance Their Activity toward Oxygen Reduction. *Nano Lett.* **2016**, *16*, 1467–1471.

(22) Wu, J.; Qi, L.; You, H.; Gross, A.; Li, J.; Yang, H. Icosahedral Platinum Alloy Nanocrystals with Enhanced Electrocatalytic Activities. *J. Am. Chem. Soc.* **2012**, *134*, 11880–11883.

(23) Cui, C.; Gan, L.; Li, H.-H.; Yu, S.-H.; Heggen, M.; Strasser, P. Octahedral PtNi Nanoparticle Catalysts: Exceptional Oxygen Reduction Activity by Tuning the Alloy Particle Surface Composition. *Nano Lett.* **2012**, *12*, 5885–5889.

(24) Ortiz, N.; Weiner, R. G.; Skrabalak, S. E. Ligand-Controlled Co-Reduction versus Electroless Co-Deposition: Synthesis of Nanodendrites with Spatially Defined Bimetallic Distributions. *ACS Nano* **2014**, *8*, 12461–12467.

(25) Zhou, M.; Wang, H.; Vara, M.; Hood, Z. D.; Luo, M.; Yang, T.-H.; Bao, S.; Chi, M.; Xiao, P.; Zhang, Y.; Xia, Y. Quantitative Analysis of the Reduction Kinetics Responsible for the One-Pot Synthesis of Pd-Pt Bimetallic Nanocrystals with Different Structures. *J. Am. Chem. Soc.* **2016**, *138*, 12263–12270.

(26) Chen, Q.; Zhang, J.; Jia, Y.; Jiang, Z.; Xie, Z.; Zheng, L. Wet Chemical Synthesis of Intermetallic Pt₃Zn Nanocrystals via Weak Reduction Reaction Together with UPD Process and Their Excellent Electrocatalytic Performances. *Nanoscale* **2014**, *6*, 7019–7024.

(27) Durieux, G.; Gerdin, M.; Moberg, C.; Jutand, A. Rate and Mechanism of the Oxidative Addition of a Silylborane to Pt⁰ Complexes—Mechanism for the Pt-Catalyzed Silaboration of 1, 3-Cyclohexadiene. *Eur. J. Inorg. Chem.* **2008**, *2008*, 4236–4241.

(28) Gilroy, K. D.; Ruditskiy, A.; Peng, H.-C.; Qin, D.; Xia, Y. Bimetallic Nanocrystals: Syntheses, Properties, and Applications. *Chem. Rev.* **2016**, *116*, 10414–10472.

(29) Blöchl, P. E. Projector Augmented-Wave Method. *Phys. Rev. B* **1994**, *50*, 17953–17979.

(30) Kresse, G.; Joubert, D. From Ultrasoft Pseudopotentials to the Projector Augmented-Wave Method. *Phys. Rev. B* **1999**, *59*, 1758–1775.

(31) Perdew, J. P.; Wang, Y. Accurate and Simple Analytic Representation of the Electron-Gas Correlation Energy. *Phys. Rev. B* **1992**, *45*, 13244–13249.

(32) Kresse, G.; Furthmüller, J. Efficient Iterative Schemes for Ab Initio Total-Energy Calculations Using a Plane-Wave Basis Set. *Phys. Rev. B* **1996**, *54*, 11169–11186.

(33) Kresse, G.; Furthmüller, J. Efficiency of Ab-Initio Total Energy Calculations for Metals and Semiconductors Using a Plane-Wave Basis Set. *Comput. Mater. Sci.* **1996**, *6*, 15–50.

(34) Haynes, W. M.; Bruno, T. J.; Lide, D. R., Eds. CRC Handbook of Chemistry and Physics, 96th ed.; CRC Press: Boca Raton, FL, **2016**.

(35) Vara, M.; Roling, L. T.; Wang, X.; Elnabawy, A. O.; Hood, Z. D.; Chi, M.; Mavrikakis, M.; Xia, Y. Understanding the Thermal Stability of Palladium-Platinum Core-Shell Nanocrystals by In Situ Transmission Electron Microscopy and Density Functional Theory. *ACS Nano* **2017**, *11*, 4571–4581.

(36) Monkhorst, H. J.; Pack, J. D. Special Points for Brillouin-Zone Integrations. *Phys. Rev. B* **1976**, *13*, 5188–5192.

(37) Henkelman, G.; Uberuaga, B. P.; Jónsson, H. A Climbing Image Nudged Elastic Band Method for Finding Saddle Points and Minimum Energy Paths. *J. Chem. Phys.* **2000**, *113*, 9901–9904.

(38) Neugebauer, J.; Scheffler, M. Adsorbate-Substrate and Adsorbate-Adsorbate Interactions of Na and K Adlayers on Al(111). *Phys. Rev. B* **1992**, *46*, 16067–16080.

(39) Bengtsson, L. Dipole Correction for Surface Supercell Calculations. *Phys. Rev. B* **1999**, *59*, 12301–12304.

(40) Ruban, A. V.; Skriver, H. L.; Nørskov, J. K. Surface Segregation Energies in Transition-Metal Alloys. *Phys. Rev. B* **1999**, *59*, 15990–16000.

(41) Nørskov, J. K.; Rossmeisl, J.; Logadottir, A.; Lindqvist, L.; Kitchin, J. R.; Bligaard, T.; Jónsson, H. Origin of the Overpotential for Oxygen Reduction at a Fuel-Cell Cathode. *J. Phys. Chem. B* **2004**, *108*, 17886–17892.

(42) Greeley, J.; Rossmeisl, J.; Hellmann, A.; Nørskov, J. K. Theoretical Trends in Particle Size Effects for the Oxygen Reduction Reaction. *Z. Phys. Chem.* **2007**, *221*, 1209–1220.

(43) Luty-Błocho, M.; Paclawski, K.; Wojnicki, M.; Fitzner, K. The Kinetics of Redox Reaction of Gold(III) Chloride Complex Ions with L-ascorbic Acid. *Inorg. Chim. Acta* **2013**, *395*, 189–196.

(44) LaMer, V. K.; Dinegar, R. H. Theory, Production and Mechanism of Formation of Monodispersed Hydrosols. *J. Am. Chem. Soc.* **1950**, *72*, 4847–4854.

(45) Wang, Y.; Peng, H.-C.; Liu, J.; Huang, C. Z.; Xia, Y. Use of Reduction Rate as a Quantitative Knob for Controlling the Twin Structure and Shape of Palladium Nanocrystals. *Nano Lett.* **2015**, *15*, 1445–1450.

(46) Xia, Y.; Xiong, Y.; Lim, B.; Skrabalak, S. E. Shape-Controlled Synthesis of Metal Nanocrystals: Simple Chemistry Meets Complex Physics? *Angew. Chem., Int. Ed.* **2009**, *48*, 60–103.

(47) Wang, X.; Vara, M.; Luo, M.; Huang, H.; Ruditskiy, A.; Park, J.; Bao, S.; Liu, J.; Howe, J.; Chi, M.; Xie, Z.; Xia, Y. Pd@Pt Core-Shell Concave Decahedra: A Class of Catalysts for the Oxygen Reduction Reaction with Enhanced Activity and Durability. *J. Am. Chem. Soc.* **2015**, *137*, 15036–15042.

(48) Wang, Y.; Xie, S.; Liu, J.; Park, J.; Huang, C. Z.; Xia, Y. Shape-Controlled Synthesis of Palladium Nanocrystals: A Mechanistic Understanding of the Evolution from Octahedrons to Tetrahedrons. *Nano Lett.* **2013**, *13*, 2276–2281.

(49) Kitchin, J. R.; Nørskov, J. K.; Barteau, M. A.; Chen, J. G. Role of Strain and Ligand Effects in the Modification of the Electronic and Chemical Properties of Bimetallic Surfaces. *Phys. Rev. Lett.* **2004**, *93*, 156801–156804.

(50) Mavrikakis, M.; Hammer, B.; Nørskov, J. K. Effect of Strain on the Reactivity of Metal Surfaces. *Phys. Rev. Lett.* **1998**, *81*, 2819–2822.

(51) Wu, J.; Li, P.; Pan, Y.-T.; Warren, S.; Yin, X.; Yang, H. Surface Lattice-Engineered Bimetallic Nanoparticles and Their Catalytic Properties. *Chem. Soc. Rev.* **2012**, *41*, 8066–8074.

(52) Inzelt, G.; Berkes, G. G.; Kriston, A. Two Types Dissolution of Platinum in Acid Media. An Electrochemical Nanogravimetric Study. *ECS Trans.* **2010**, *25*, 137–156.

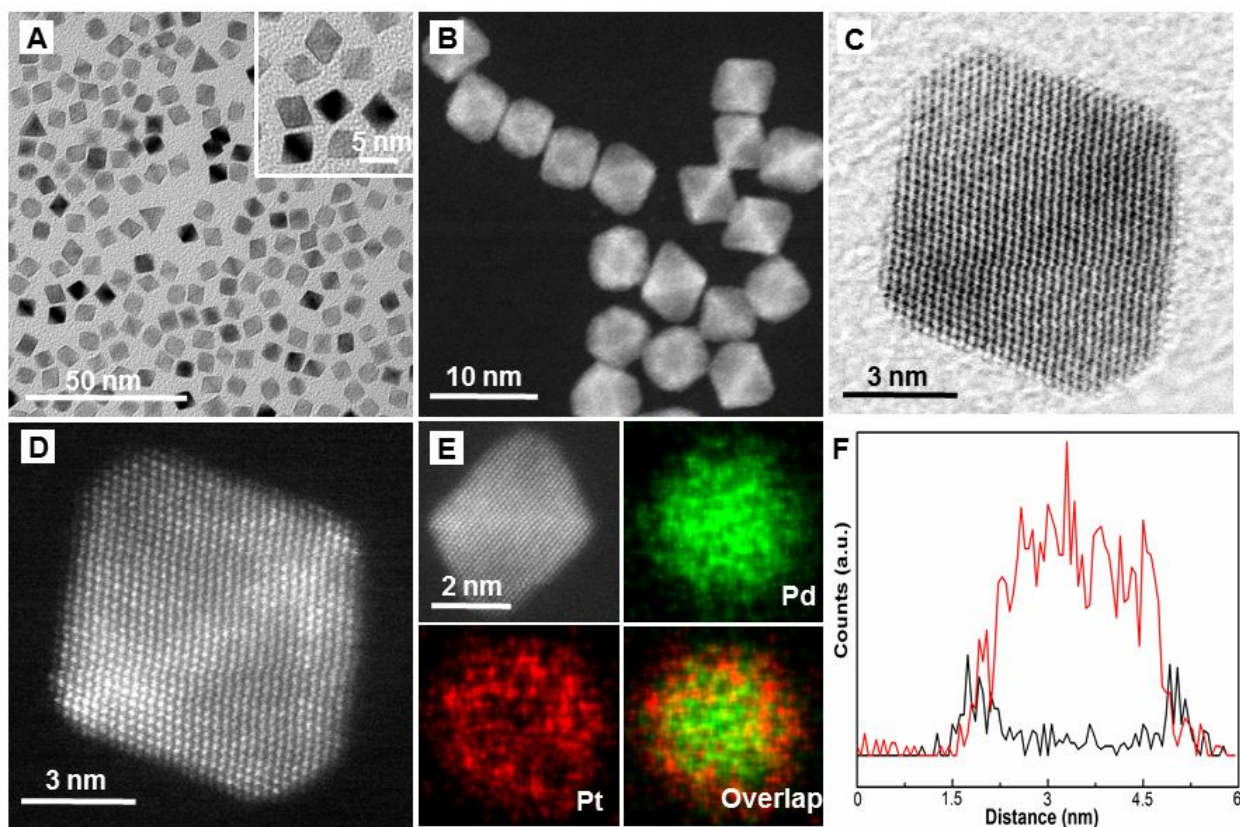


Figure 1. (A) TEM and (B) low-magnification HAADF-STEM images of Pd@Pt_{IL} octahedral nanocrystals. (C) Bright-field STEM and (D) atomic-resolution HAADF-STEM images taken from an individual Pd@Pt_{IL} octahedron. (E) HAADF-STEM image of a Pd@Pt_{IL} octahedron and the corresponding EDX mapping of Pd and Pt. (F) EDX line scans of Pd (red trace) and Pt (black trace) recorded from a Pd@Pt_{IL} octahedron.

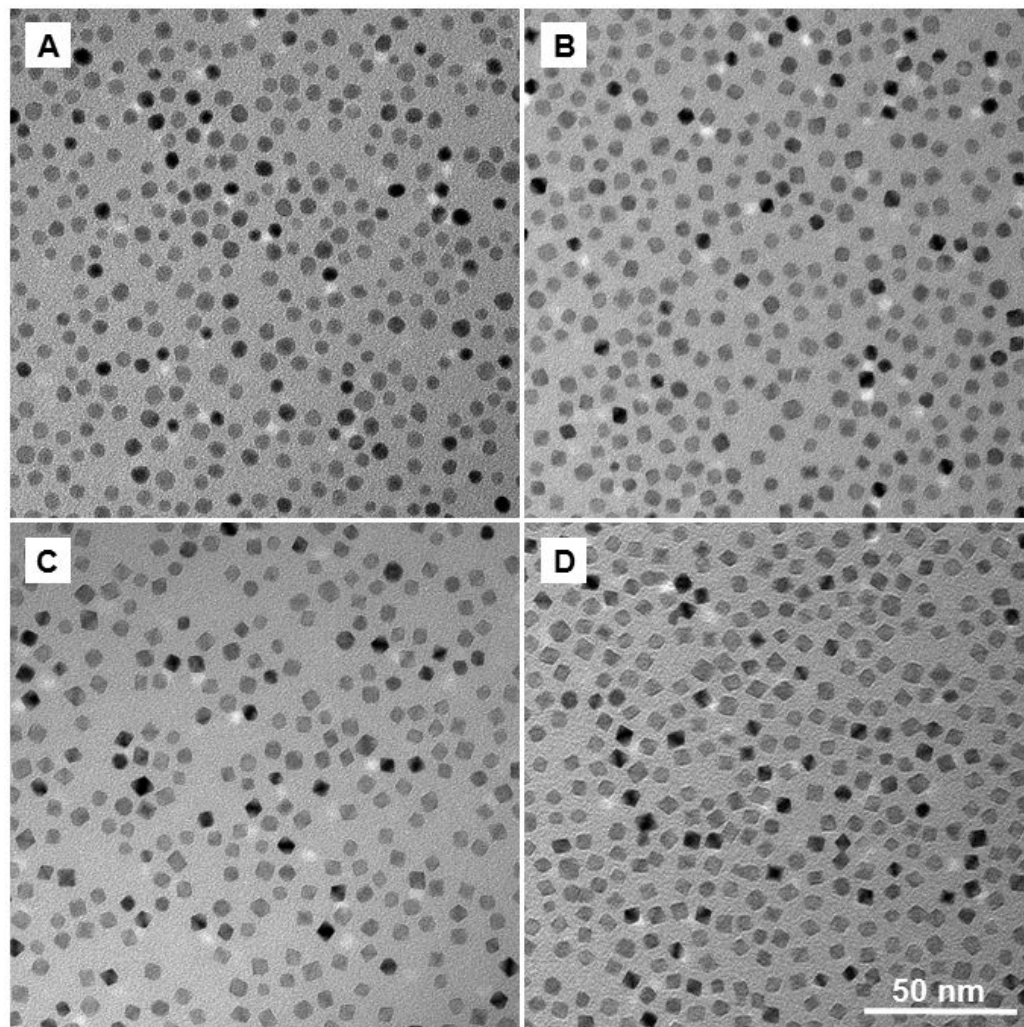


Figure 2. TEM images of the Pd@Pt_{1L} octahedral nanocrystals synthesized using the standard protocol except for the difference in reaction time: (A) 2, (B) 20, (C) 60, and (D) 120 min.

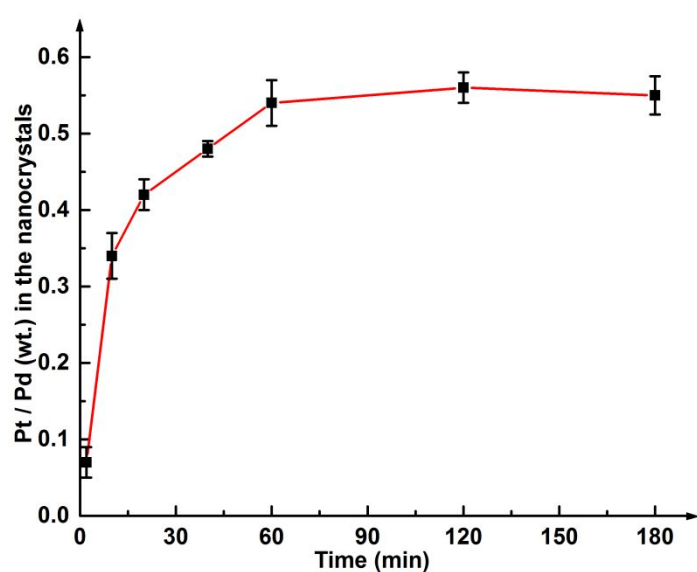


Figure 3. Plot showing the mass ratio of Pt to Pd, determined using ICP-MS analysis, as a function of reaction time for the samples shown in Figure 2.

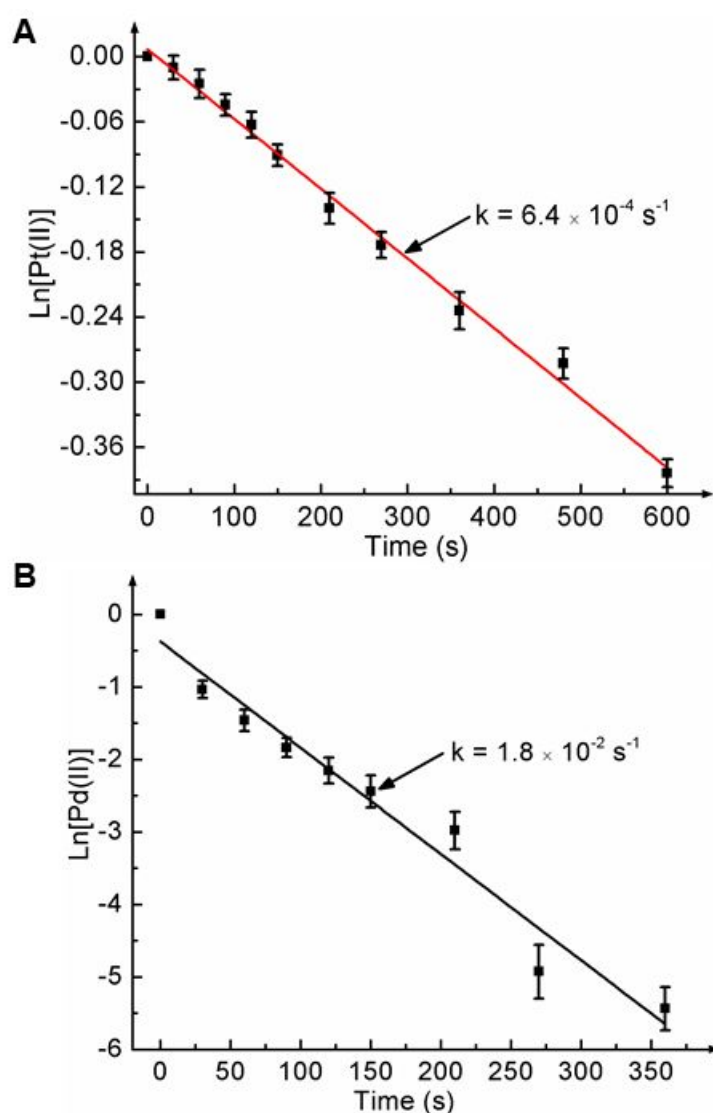


Figure 4. Quantitative analysis of the reduction kinetics involved in the standard synthesis of Pd@Pt_{IL} octahedral nanocrystals. Plots of (A) $\ln[\text{Pt(II)}]$ and (B) $\ln[\text{Pd(II)}]$ as a function of reaction time, respectively, giving straight lines whose slopes correspond to the pseudo-first-order rate constants. Note that the concentrations used to construct these plots were normalized to the initial concentration.

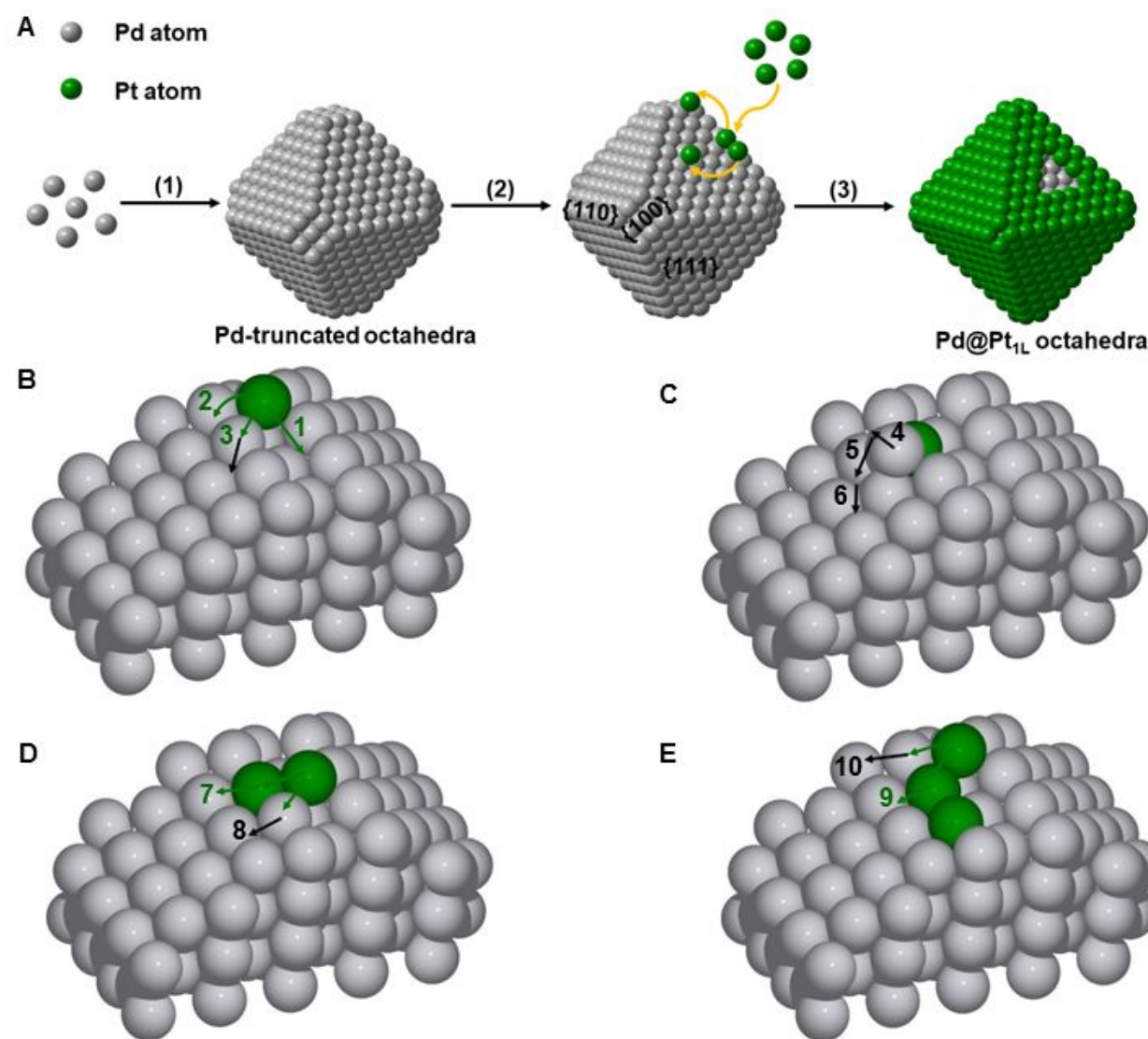


Figure 5. (A) Schematic illustration of the growth mechanism of Pd@Pt_{1L} octahedral nanocrystals: (1) nucleation and growth of Pd octahedra with truncation at the corners; (2) selective deposition of Pt atoms on the edges of the Pd truncated octahedra; (3) surface diffusion of the deposited Pt atoms to generate Pd@Pt_{1L} octahedra with sharp corners. (B–E) DFT calculated pathways for Pt and Pd diffusion across the edge model: green and black arrows represent diffusion (*via* hopping or substitution) of a Pt atom and a Pd atom, respectively.

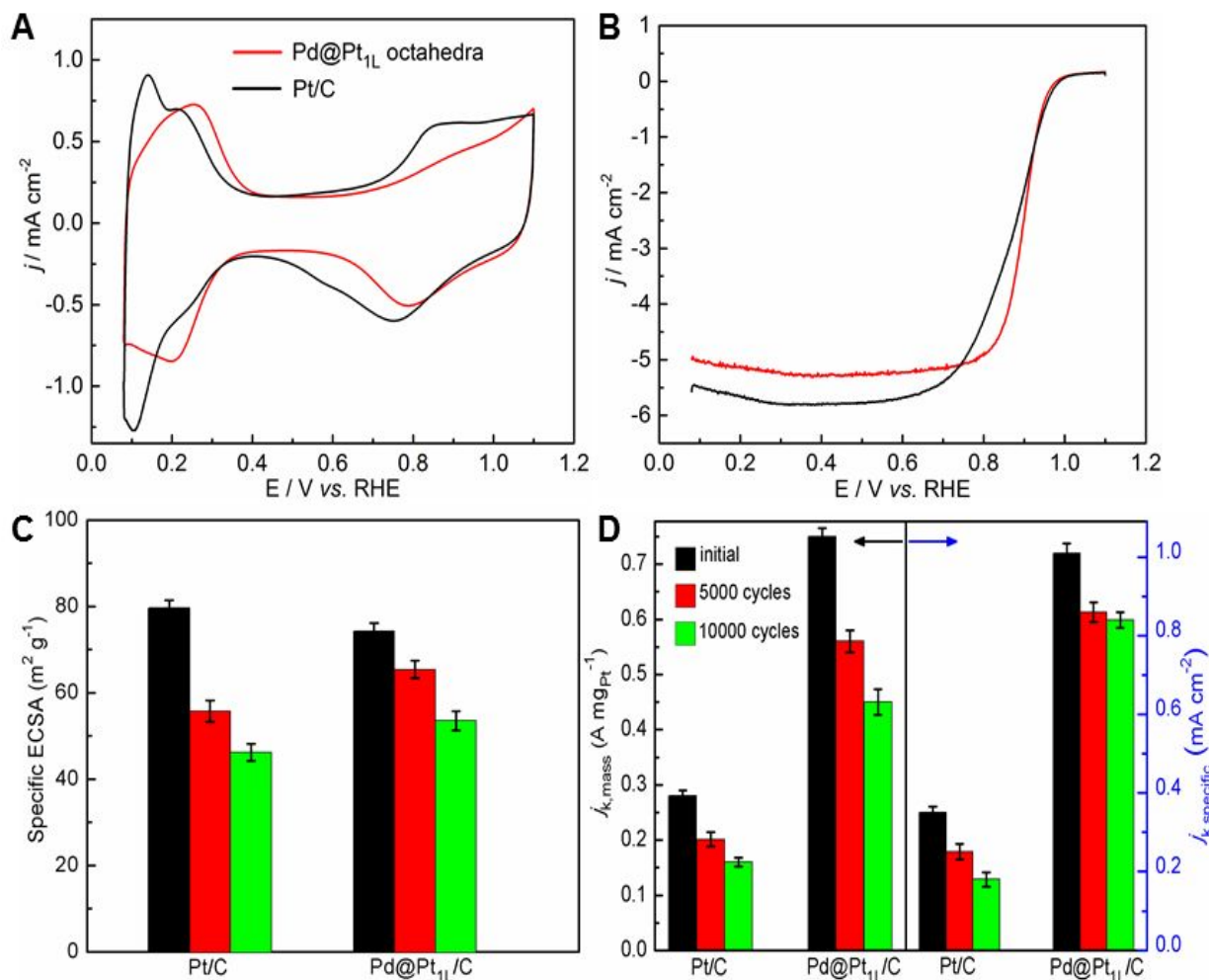


Figure 6. Electrochemical properties of the carbon-supported Pd@Pt_{1L} octahedra, benchmarked against the Pt/C catalyst. (A) CVs of the catalysts in a N₂-saturated HClO₄ solution at room temperature. (B) Positive-going ORR polarization curves of the catalysts in an O₂-saturated HClO₄ solution. Durability tests for the carbon-supported Pd@Pt_{1L} octahedra and the Pt/C catalyst. The comparison is based on (C) the specific ECSA and (D) the mass and specific ORR activity at 0.9 V_{RHE} for the catalysts before and after the accelerated durability test. The color scheme specified in (D) applies to panel (C).

1
2
3 **Table 1.** Calculated activation energy barriers (E_a) and diffusion energies (ΔE) for the diffusion
4 processes involving Pt and Pd atoms depicted in Figure 5, B–E. All energies are in eV.
5
6

Pathway	Description	E_a	ΔE
1	Pt atom hops from one {110} hollow site to another	0.57	0.00
2	Pt atom at a {110} hollow site hops above the Pd trough onto an fcc site on the adjacent {111} terrace	1.59	0.83
3	Pt atom at a {110} hollow site substitutes a neighboring Pd trough atom, thus pushing it onto an <i>fcc</i> site on the adjacent {111} terrace	0.66	0.37
4	Pd atom hops away from the {110} edge across the {111} terrace from an <i>fcc</i> to an <i>hcp</i> site	0.06	0.02
5	Pd atom hops away from the {110} edge across the {111} terrace from the previous <i>hcp</i> to another <i>fcc</i> site	0.25	0.17
6	Pd atom hops away from the {110} edge across the {111} terrace from the previous <i>fcc</i> to another <i>hcp</i> site	0.12	0.07
7	Pt atom in a {110} hollow site substitutes a neighboring Pt trough atom, thus pushing it onto an <i>fcc</i> site on the adjacent {111} terrace	1.08	0.80
8	Pt atom in a {110} hollow site substitutes a second Pd trough atom, thus pushing it onto an <i>fcc</i> site on the adjacent {111} terrace	0.82	0.50
9	Pt atom in a {110} hollow site substitutes a neighboring Pt trough atom, thus pushing it onto an <i>fcc</i> site on the adjacent {111} terrace	1.09	0.76
10	Pt atom in a {110} hollow site substitutes a third Pd trough atom, thus pushing it onto an <i>hcp</i> site on the adjacent {111} terrace	0.91	0.51

TOC

